



Contra-directional switching enabled by Si-GST grating

HAO HU,¹ HANYU ZHANG,¹  LINJIE ZHOU,^{1,*} JIAN XU,² LIANGJUN LU,¹  JIANPING CHEN,¹ AND B. M. A. RAHMAN³

¹State Key Laboratory of Advanced Optical Communication Systems and Networks, Shanghai Institute for Advanced Communication and Data Science, Department of Electronic Engineering, Shanghai Jiao Tong University, Shanghai 200240, China

²Center of Advanced Electronic Materials and Devices, Shanghai Jiao Tong University, Shanghai 200240, China

³Department of Electrical and Electronic Engineering, City, University of London, London EC 1 V 0HB, United Kingdom

*ljzhou@sjtu.edu.cn

Abstract: We present the design, simulation, and experimental demonstration of a Si-GST grating assisted contra-directional coupler for optical switching. The effective refractive index of the GST-loaded silicon waveguide changes significantly when the GST is switched from the amorphous state to the crystalline state, allowing for large tuning of the propagation constant. The two coupled waveguides are designed to satisfy the phase-match condition only at the amorphous state to achieve Bragg reflection at the drop-port. Experimental results show that the device insertion loss is less than 5 dB and the extinction ratio is more than 15 dB with an operation bandwidth of 2.2 nm around the 1576 nm operating wavelength. Due to the nonvolatile property of GST, there is no static power consumption to maintain the two states. It is the first demonstration of a GST-enabled grating coupler that can be switched by phase change material.

© 2020 Optical Society of America under the terms of the [OSA Open Access Publishing Agreement](#)

1. Background

In recent years, photonic devices on the silicon-on-insulator (SOI) platform have been intensively investigated and seen rapid development [1–3]. Multiple photonic devices and integrated circuits have been realized using CMOS-compatible processes, including optical filters [4], electro-optic modulators [5], large-scale optical switches [6], and microwave signal processors [7–10]. To integrate more functions in one single chip for high-density integration, it is required to reduce the individual device size and power consumption. Although highly-compact passive devices have been developed by making use of the inverse design [11], the actively tunable devices are still of large volume and power-hungry. In general, silicon active photonic devices routinely use the thermo-optic (TO) effect or the free-carrier dispersion (FCD) effect to achieve refractive index (RI) modulation. However, the RI variation is relatively small and a long active waveguide length is required to attain a π phase shift, as often demanded in optical switches and modulators. Although resonant and slow-light structures can enhance the tuning sensitivity, they sacrifice the optical bandwidth, making the device less tolerable to fabrication imperfections and more sensitive to temperature fluctuations. Moreover, the TO and FCD effects are both volatile, implying that constant power supply is required to maintain the RI change. It consumes considerable static power, especially for a photonic chip containing multiple active devices.

Ge₂Sb₂Te₅ (GST), as a well-known phase change material (PCM), can change the phase between the amorphous state (a-gst) and the crystalline state (c-gst) with a large RI contrast [12,13]. The phase change is non-volatile and highly repeatable. By combining GST and silicon waveguides, we can exploit the phase change property of GST to actively tune the silicon waveguides, allowing for high-density and low-power operation. In fact, research on PCMs

has been carried out for many years. It has been demonstrated that the phase change can be induced thermally [14,15], optically [16–19], or electrically [20–23] potentially with high speed. In the crystallization process, the GST is heated above the phase transition temperature and then slowly cooled down [24]. On the other hand, for amorphization, the GST is heated up to the melting temperature and then quenched rapidly. In terms of functionalities, Si-GST hybrid waveguides can be used for optical switching [20,21,24–26,26], electro-optic modulation [27], non-volatile optical memory [28–30] and optical computing [31–33] due to its superior electrical and optical characteristics. These demonstrations indicate that the Si-GST hybrid integration is quite promising for photonic integrated circuits to satisfy versatile applications.

Previously, Si-GST based 1×2 and 2×2 directional couplers have been demonstrated [34,35]. Compared to the regular directional couplers, the grating-assisted contra-directional coupler has the characteristic that the optical power transfer between the two coupled waveguides is not periodic, but monotonically dependent on the coupling length. It means that the contra-directional coupler does not require strict control of the coupling length to get the maximum coupling as long as it is long enough. In this paper, we demonstrate a novel Si-GST grating assisted contra-directional coupler. The employment of GST makes the device digitally tunable with bi-stable states, suitable for optical switching applications. This presents, to the best of our knowledge, the first-ever demonstration of PCM-actuated contra-directional grating coupler. The paper is organized as follows. First, we present the design and simulation of the grating-assisted contra-directional coupler. Next, we describe the device fabrication process and measurement setup. We then present the experimental results and compare with the simulation. Finally, we draw conclusions.

2. Device structure and operation principle

Figure 1 shows the schematic structure of the grating-assisted contra-directional coupler. It consists of two parallel silicon strip waveguides. One waveguide has periodic corrugations with a 50% duty cycle along the inner sidewall and meanwhile covered with GST nano-strips on top. Compared to the contra-directional couplers with only the inner sidewall grating [36], the employment of both the inner sidewall grating and the surface grating can enhance the coupling strength and hence reduce the coupling length. In our device, only the surface grating is formed by GST, which makes a compromise between the insertion loss and the switching extinction ratio. Without the inner sidewall grating, the coupling is much weaker for amorphous GST, leading to a lower reflection peak due to the incomplete energy transfer on Bragg resonance. On the other hand, if the inner sidewall grating is also made of GST, then the insertion loss at the through-port becomes very large when GST turns into crystalline due to the strong mode overlap with the sidewall GST. The silicon waveguide height is $H = 220$ nm. The widths of the two waveguides are $W_1 = 370$ nm (pure silicon waveguide) and $W_2 = 400$ nm (GST-loaded silicon waveguide). The corrugation depth is $D = 50$ nm. The gap between the two waveguides is $G = 230$ nm. The GST nano-strip has dimensions of $W_{\text{GST}} = 390$ nm and $L_{\text{GST}} = 100$ nm. The GST layer thickness is $H_{\text{GST}} = 50$ nm and the GST grating period is $\Lambda = 374$ nm.

Upon phase transition of GST from the amorphous state to the crystalline state, its complex refractive index increases significantly from $n_{\text{a-gst}} = 3.903 + 0.006i$ to $n_{\text{c-gst}} = 6.077 + 0.904i$, measured by ellipsometry at the 1550 nm wavelength [15]. When GST is in the amorphous state, the phase match condition is satisfied and the input light is reflected to the drop-port. The phase match condition is expressed as

$$\beta_a(\lambda) + \beta_b(\lambda) = 2\pi/\Lambda \quad (1)$$

where β_a and β_b represent the propagation constants of the silicon waveguide and the GST-loaded silicon waveguide for the transverse electric (TE) polarization mode, respectively. The

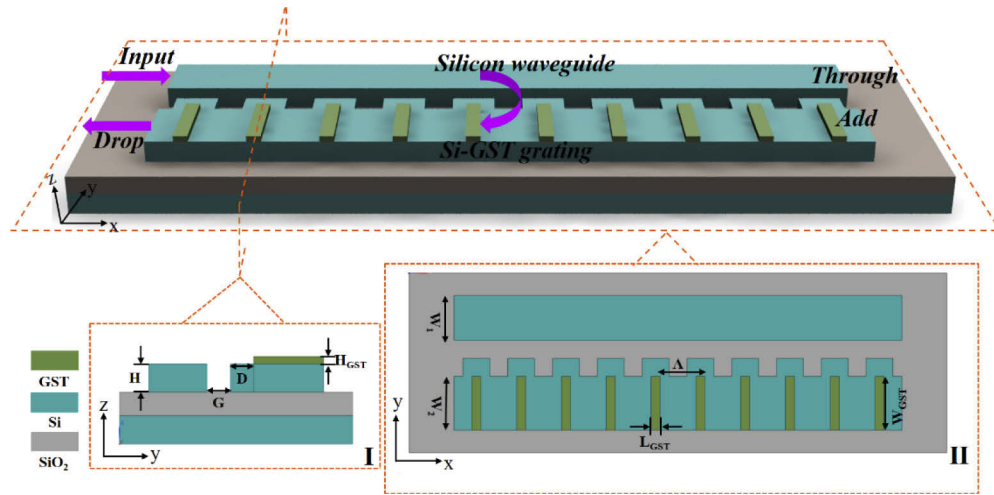


Fig. 1. Three-dimensional perspective view of the contra-directional coupler enabled by Si-GST grating. Inset I illustrates the cross-sectional view of the coupler. Inset II illustrates the top view of the coupler. The critical dimensions are labeled in the graphs.

propagation constants can be written as

$$\beta_a = 2\pi n_1/\lambda \quad \beta_b = 2\pi n_2/\lambda \quad (2)$$

where λ is the Bragg resonance wavelength, n_1 and n_2 are the effective refractive indices of the silicon waveguide and the GST-loaded silicon waveguide, respectively. Therefore, we have

$$n_1 + n_2 = \lambda/\Lambda \quad (3)$$

As the GST-loaded waveguide has a periodic pattern in the longitudinal direction, we obtain its effective refractive index n_2 by using the Rytov's formula [37]:

$$n_2^2 = n_{2-1}^2 * FF + n_{2-2}^2 * (1 - FF) \quad (4)$$

where n_{2-1} and n_{2-2} are the effective refractive indices of the waveguide sections with and without GST, respectively, and FF represents the duty cycle of the GST grating. As GST changes from the amorphous state to the crystalline state, the refractive index of GST undergoes a large change, which causes an increment of n_2 and subsequently redshift of the Bragg wavelength. Meanwhile, the extinction coefficient of GST also increases considerably, resulting in a higher loss of the GST-loaded silicon waveguide. Therefore, light comes out from the through-port with suppressed coupling to the drop-port. The contra-directional coupling coefficient of the two waveguides is obtained by the coupled-mode theory [38], written as:

$$K = \frac{\omega \epsilon_0}{4} \iint E_a \cdot \Delta n^2 E_b dx dy \quad (5)$$

where E_a and E_b are the electric field distributions in the silicon waveguide and the GST-loaded waveguide, respectively, Δn is the perturbation of the refractive index, ω is the angular frequency of light, and ϵ_0 is the dielectric constant of vacuum.

3. Numerical simulations

The input light is reflected to the drop-port only when Eq. (3) is satisfied. As both the left- and right-hand terms are wavelength dependent, the reflection only occurs around a certain

wavelength, as shown in Fig. 2. When the grating period is $\Lambda = 374$ nm, the Bragg reflection occurs at the 1550 nm wavelength.

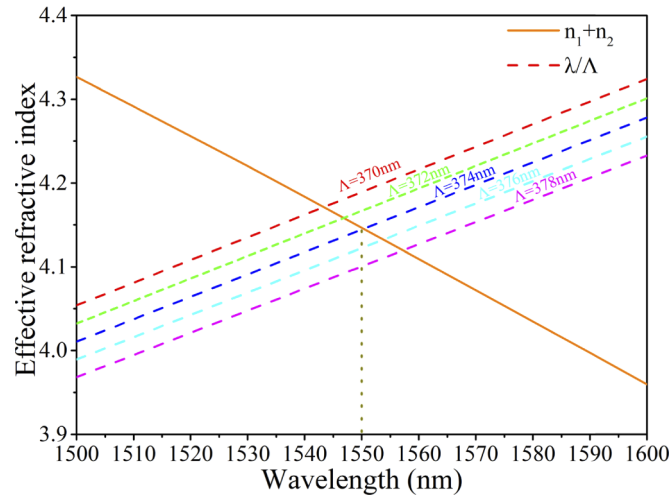


Fig. 2. Calculated effective indices of the waveguide modes with the phase-match conditions. The contra-directional coupling is only achieved at the intersection point.

We next use the finite-difference time-domain (FDTD) simulation to calculate the device performances. The length of the grating is chosen as $L = 200$ μm . In contra-directional couplers, a longer coupling length always gives a higher reflectivity. However, in our device, we also need to consider the through-transmission loss when GST becomes crystalline. Therefore, we choose a relatively conservative length to get balanced switching performances. Figure 3 shows the numerically simulated transmission spectra. The center wavelength of the Bragg reflection is about 1553 nm. At the resonance wavelength and with the amorphous GST, the insertion loss of the drop-port is 0.95 dB and the crosstalk between the two ports is about -17 dB. Here, we define the crosstalk as the power difference between the through- and drop-ports at the operation

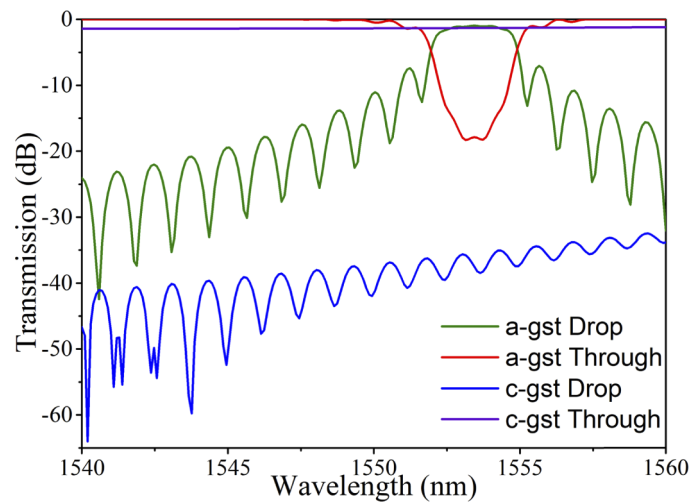


Fig. 3. Simulated through and drop transmission spectra when GST changes from the amorphous (a-gst) to the crystalline (c-gst) state.

wavelength. In terms of optical switching, the crosstalk should be kept as low as possible to purify signal transmission to a single destination port. When GST changes from the amorphous state to the crystalline state, light is hardly coupled from the first waveguide to the second waveguide, leading to low reflection to the drop-port. The insertion loss of the through-port is 1.4 dB and the crosstalk between the two ports is less than -30 dB over the simulated wavelength range.

Figures 4(a) and 4(b) show the calculated optical wave electric-field intensity distributions when GST is switched between two states at the 1553 nm wavelength. It clearly illustrates that strong reflection is only obtained when GST is in the low-loss amorphous state.

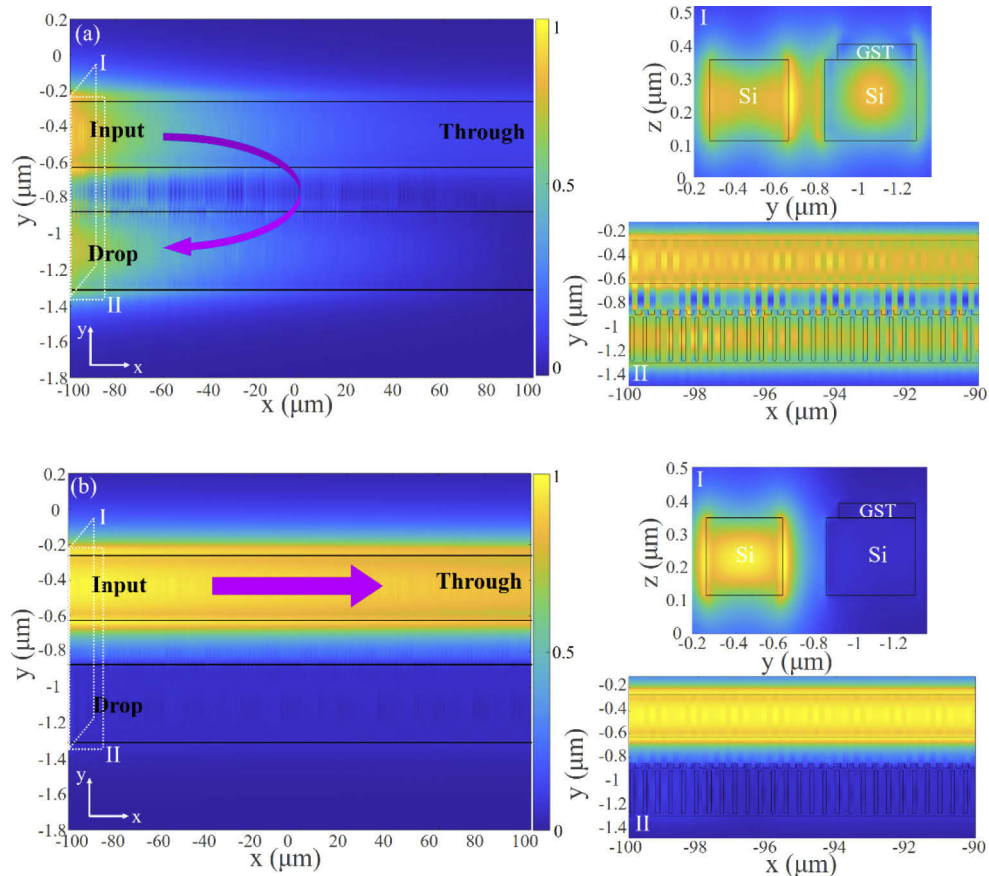


Fig. 4. Electric-field intensity ($|E|^2$) distribution in the x-y plane at the Bragg resonance wavelength when GST is in the (a) amorphous state and (b) crystalline state. Inset I: Electric-field cross-sectional profile. Inset II: Magnified view of the Electric-field intensity distribution in the front 10- μm -long section.

4. Device fabrication

The device was fabricated on a silicon-on-insulator wafer with a 220-nm-thick top silicon layer and a 2- μm -thick buried oxide layer. The silicon waveguides were patterned by electron beam lithography (EBL) and then dry-etched by inductively coupled plasma (ICP) etching. Next, poly-methyl-meth-acrylate (PMMA) resist was spin-coated and the window of the GST grating was opened using the second EBL. A 50-nm-thick GST film was deposited from a stoichiometric

$\text{Ge}_2\text{Sb}_2\text{Te}_5$ alloy target using radio frequency (RF) sputtering (20 W, 15 s.c.c.m. argon gas). Finally, The GST was patterned using the lift-off process in a warm acetone bath.

Figure 5 shows the optical microscope image and the magnified scanning electron microscope (SEM) image of the fabricated device. Since the chip temperature during sputtering is lower than the GST phase transition temperature, the GST is initially in the amorphous state. In order to convert the GST to the crystalline state, we heated it on a hot plate with 245 °C temperature for 5 minutes.

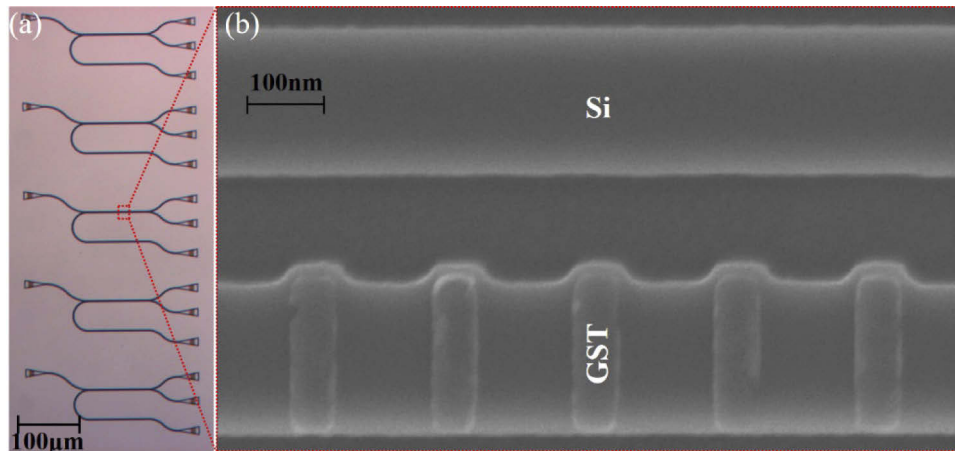


Fig. 5. (a) Optical microscope image of the fabricated devices with different grating periods. (b) Scanning electron microscope image of the coupling region.

5. Experimental results

We measured the transmission spectrum of the devices using a tunable laser (Agilent 81600B) scanning from 1500 nm to 1640 nm with a step size of 5 pm and an optical power monitor (Agilent 81636B). The polarization was adjusted to the quasi-TE mode using a polarization controller. The light was coupled into and out of the device through on-chip vertical grating couplers using two single-mode fibers mounted at an angle of about 10°. The vertical grating couplers have an etched depth of 70 nm. The measured transmission spectra were all normalized to a reference straight waveguide.

Figure 6 shows the transmission spectra of the through- and drop-ports at four grating periods of 370 nm, 374 nm, 378 nm, and 382 nm when the GST nano-strips are at the amorphous state. As the grating period in the contra-directional coupler increases, the resonance wavelength undergoes redshift from 1561.7 nm, 1569.65 nm, 1581 nm, to 1592 nm. The through-port has an average insertion loss of 2.5 dB outside the reflection band. Pronounced resonance notches can be discerned. The drop-port has an insertion loss of 0.5-1.5 dB in the reflection band. The 3-dB bandwidth is around 5 nm. The crosstalk between the through-port and the drop-port at the resonance wavelengths are -27.3 dB, -32 dB, -31.5 dB, and -29 dB for the four devices, respectively. As the grating is uniform, strong sidelobes can be observed in the drop spectrum outside the reflection band, which is also present in the simulation results. The irregularity of the sidelobes is probably due to the size variation and edge roughness of the GST nano-strips since we used the lift-off process to pattern the GST grating. The sidelobes can be suppressed by using an apodized grating design, in which the coupling strength is tapered between the forward-propagating wave and the backward-propagating wave [39]. Compared to the simulation results of Fig. 3, we find that the Bragg wavelength is redshifted with broader bandwidth and

lower crosstalk. We attribute this discrepancy to the increased GST thickness. A thicker GST nano-strip layer results in a larger coupling coefficient, and therefore lower crosstalk and larger bandwidth.

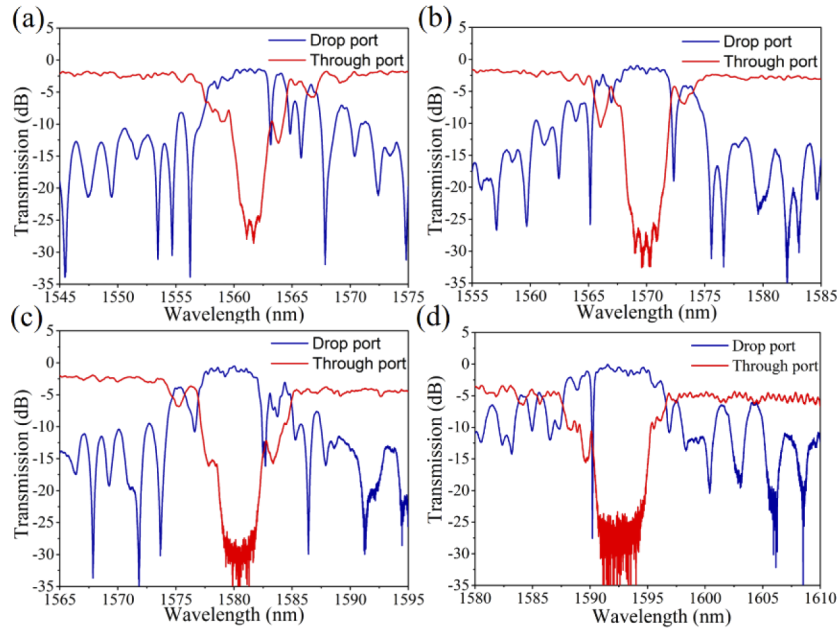


Fig. 6. Measured transmission spectra of devices when the GST is at the amorphous state with grating periods of (a) 370 nm, (b) 374 nm, (c) 378 nm, and (d) 382 nm.

Figure 7 shows the measured transmission spectra with GST at the amorphous and crystalline states when the GST grating period was $\Lambda=376$ nm. When GST is in the amorphous state, the resonance wavelength is at 1576 nm. The notch in the through-port spectrum has a depth of 25 dB and the peak transmission loss of the drop-port is about 3.4 dB. When GST changes to the crystalline state, the contra-directional resonance wavelength is redshifted by 1.8 nm and meanwhile, the reflection to the drop-port is greatly weakened. The notch depth in the

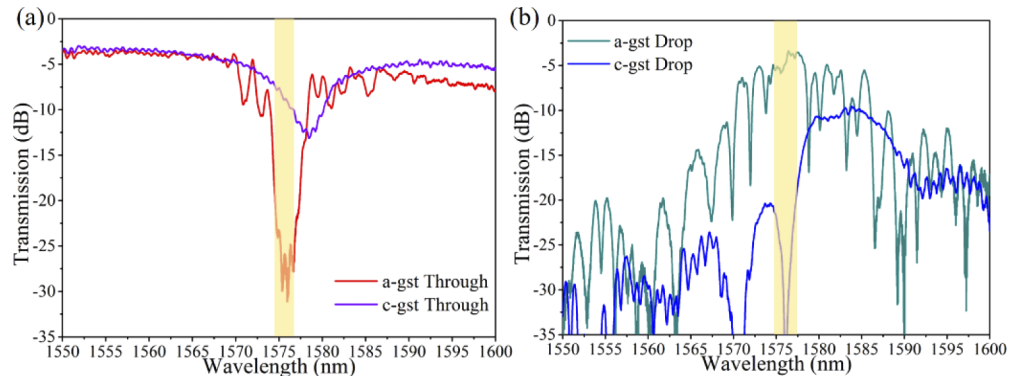


Fig. 7. Measured spectra at (a) the through-port and (b) the drop-port when GST changes from the amorphous state to the crystalline state. The yellow bar indicates the 2.2 nm operation bandwidth for optical switching.

through-port is reduced to 8 dB and the peak transmission loss of the drop-port is increased to 10 dB. Compared to the simulation results, both the resonance wavelength shift and the notch depth change are smaller. This is probably because the refractive index of the crystalline state GST used in the simulation is larger than that in the real devices. For optical switching applications, the operating wavelength can be set to the original Bragg resonance wavelength, i.e., 1576 nm. Over a bandwidth of 2.2 nm, the switching extinction ratio, defined as the power difference between the amorphous and crystalline GST states, are larger than 15 dB for both through- and drop-ports.

6. Discussion

In the above proof-of-principle demonstration, we adopt the uniform grating design. As well known, the uniform grating would inevitably generate strong side lobes. The sidelobe rejection ratio in our design is only 6.5 dB, as seen in Fig. 3. Apodization is a common method to suppress sidelobes. Here, we apodize the duty cycle of the grating with a Gaussian-cosine function to keep n_2 constant [40]. The formula for duty cycle modulation is expressed as

$$FF(i) = FF_0 + (1 - e^{-\frac{a(i-N/2)^2}{N^2}}) * \cos(i\pi) * FF_0 \quad (6)$$

where N is the number of grating periods, FF_0 is the duty cycle of the uniform grating, a is the apodization coefficient that determines the shape of the apodized grating. Increasing the apodization coefficient will increase sidelobe suppression. However, it also results in a lower reflection peak. Figure 8 shows the transmission spectra of the apodized grating ($a = 8$) and the original uniform grating for comparison. It can be seen that the sidelobe rejection ratio is increased to 18 dB. The peak reflection can be increased by using a longer coupler.

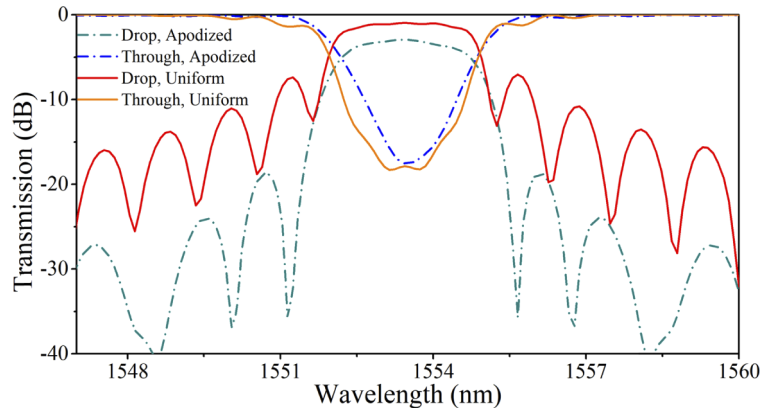


Fig. 8. Comparison of the transmission spectra of two contra-directional couplers with apodized and uniform gratings, respectively.

One way to make the phase change of GST is to use free-space optical beam writing [34]. A pulsed pump laser can be incident from the device normal direction and focused onto one GST cell. When enough pump light power is absorbed by GST, its temperature can be raised rapidly. By controlling the pulse energy, reversible phase change can be obtained. The pulse energy for GST phase transition from crystalline to amorphous and the reverse is 9 aJ/nm³ and 3 aJ/nm³, respectively. Therefore, the energy consumption for our grating device with 540 GST cells is around 9.5 nJ and 3.2 nJ. Alternatively, we can also integrate a silicon resistive microheater nearby the Si-GST grating waveguide as shown conceptually in Fig. 9. The slab layer on the outer side of the Si-GST grating is heavy n++ doped, which thereby forms a silicon resistor. When electrical pulses are applied to the resistor, heat will be generated and raise the temperature of GST to realize phase change.

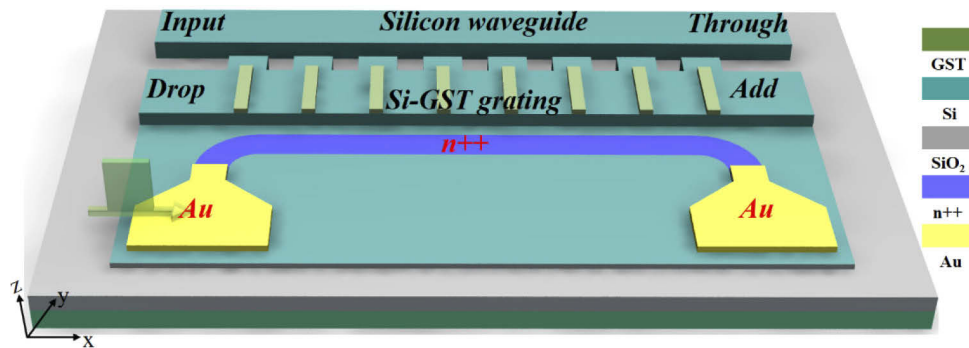


Fig. 9. Scheme for electrically driven contra-directional switching by integrating a silicon resistive microheater in the vicinity of the Si-GST grating.

7. Conclusions

We have demonstrated a grating-assisted contra-directional coupler based on the Si-GST hybrid integration technology. The device can work as a 1×2 wavelength-selective optical switch. We implemented a group of devices with various grating periods. At the amorphous state, the through-port exhibits a 25-dB-deep resonance notch and the drop-port has a peak transmission loss of 3.4 dB. GST changes from the amorphous state to the crystalline state when the device is heated up to its phase transition temperature, resulting in a greatly suppressed Bragg resonance. The switching extinction ratios of the through- and drop-ports exceed 15 dB in a 2.2 nm operation bandwidth centered at 1576 nm wavelength. Thanks to the self-holding effect of GST, no power is required to maintain the two states. These results open a significant new space of design freedom – the incorporation of PCM in silicon photonics as an efficient non-volatile tuner, which can have applications in digital optical switches, reconfigurable optical circuits, and neuromorphic photonic networks.

Funding

National Natural Science Foundation of China (61535006, 61705129); National Basic Research Program of China (973 Program) (2018YFB2201702, 2019YFB2203203); Science and Technology Commission of Shanghai Municipality (2017SHZDZX0).

Acknowledgments

The authors thank the Center for Advanced Electronic Materials and Devices (AEMD) of Shanghai Jiao Tong University (SJTU) for support in device fabrications.

Disclosures

The authors declare no conflicts of interest.

References

1. D. Po, Y. K. Chen, G. H. Duan, and T. N. David, "Silicon photonic devices and integrated circuits," *Nanophotonics* **3**(4-5), 215–228 (2014).
2. H. Subbaraman, X. Xu, A. Hosseini, X. Zhang, Y. Zhang, D. Kwong, and R. T. Chen, "Recent advances in silicon-based passive and active optical interconnects," *Opt. Express* **23**(3), 2487–2511 (2015).
3. D. Thomson, A. Zilkie, J. E. Bowers, T. Komljenovic, G. T. Reed, L. Vivien, D. Marris-Morini, E. Cassan, L. Viot, and J. Fédéli, "Roadmap on silicon photonics," *J. Opt.* **18**(7), 073003 (2016).
4. L. Shen, L. Lu, Z. Guo, L. Zhou, and J. Chen, "Silicon optical filters reconfigured from a 16×16 Benes switch matrix," *Opt. Express* **27**(12), 16945–16957 (2019).

5. Y. Zhou, L. Zhou, F. Su, X. Li, and J. Chen, "Linearity measurement and pulse amplitude modulation in a silicon single-drive push-pull Mach-Zehnder modulator," *J. Lightwave Technol.* **34**(14), 3323–3329 (2016).
6. Z. Guo, L. Lu, L. Zhou, L. Shen, and J. Chen, "16×16 silicon optical switch based on dual-ring assisted Mach-Zehnder interferometers," *J. Lightwave Technol.* **36**(2), 225–232 (2018).
7. G. Zhou, L. Zhou, L. Lu, Y. Guo, and J. Chen, "Phase-coded microwave signal generation based on a segmented silicon Mach-Zehnder modulator," *IEEE J. Sel. Top. Quantum Electron.* **26**(2), 1–8 (2020).
8. F. Zhou, H. Chen, X. Wang, L. Zhou, J. Dong, and X. Zhang, "Photonic Multiple Microwave Frequency Measurement Based on Frequency-to-Time Mapping," *IEEE Photonics J.* **10**(2), 1–7 (2018).
9. Q. Sun, L. Zhou, L. Lu, G. Zhou, and J. Chen, "Reconfigurable High-Resolution Microwave Photonic Filter Based on Dual-Ring-Assisted MZIs on the Si₃N₄ Platform," *IEEE Photonics J.* **10**(6), 1–12 (2018).
10. Y. Zhong, L. Zhou, Y. Zhou, Y. Xia, S. Liu, L. Lu, J. Chen, and X. Wang, "Microwave frequency upconversion employing a coupling-modulated ring resonator," *Photonics Res.* **5**(6), 689 (2017).
11. A. Y. Piggot, J. Lu, K. G. Lagoudakis, J. Petykiewicz, T. M. Babinec, and J. Vuckovic, "Inverse design and demonstration of a compact and broadband on-chip wavelength demultiplexer," *Nat. Photonics* **9**(6), 347–350 (2015).
12. M. Wuttig, H. Bhaskaran, and T. Taubner, "Phase-change materials for non-volatile photonic applications," *Nat. Photonics* **11**(8), 465–476 (2017).
13. T. Moriyama, D. Tanaka, P. Jain, H. Kawashima, M. Kuwahara, X. Wang, and H. Tsuda, "Ultra-compact, self-holding asymmetric Mach-Zehnder interferometer switch using Ge₂Sb₂Te₅ phase-change material," *IEICE Electron. Express* **11**(15), 20140538 (2014).
14. M. Stegmaier, C. Ríos, H. Bhaskaran, and W. H. P. Pernice, "Thermo-optical effect in phase-change nanophotonics," *ACS Photonics* **3**(5), 828–835 (2016).
15. H. Zhang, L. Zhou, B. M. A. Rahman, X. Wu, L. Lu, Y. Xu, J. Xu, J. Song, Z. Hu, L. Xu, and J. Chen, "Ultracompact Si-GST hybrid waveguides for nonvolatile light wave manipulation," *IEEE Photonics J.* **10**(1), 1–10 (2018).
16. M. Rudé, J. Pello, R. E. Simpson, J. Osmond, G. Roelkens, J. J. G. M. van der Tol, and V. Pruneri, "Optical switching at 1.55µm in silicon racetrack resonators using phase change materials," *Appl. Phys. Lett.* **103**(14), 141119 (2013).
17. D. Tanaka, Y. Shoji, M. Kuwahara, X. Wang, K. Kintaka, H. Kawashima, T. Toyosaki, Y. Ikuma, and H. Tsuda, "Ultra-small, self-holding, optical gate switch using Ge₂Sb₂Te₅ with a multi-mode Si waveguide," *Opt. Express* **20**(9), 10283–10294 (2012).
18. Y. Ikuma, Y. Shoji, M. Kuwahara, X. Wang, K. Kintaka, H. Kawashima, D. Tanaka, and H. Tsuda, "Reversible optical gate switching in Si wire waveguide integrated with Ge₂Sb₂Te₅ thin film," *Electron. Lett.* **46**(21), 1460 (2010).
19. H. Zhang, L. Zhou, J. Xu, L. Lu, J. Chen, and B. M. A. Rahman, "All-optical non-volatile tuning of an AMZI-coupled ring resonator with GST phase-change material," *Opt. Lett.* **43**(22), 5539–5542 (2018).
20. K. Kato, M. Kuwahara, H. Kawashima, T. Tsuruoka, and H. Tsuda, "Current-driven phase-change optical gate switch using indium-tin-oxide heater," *Appl. Phys. Express* **10**(7), 072201 (2017).
21. F. Xiong, A. D. Liao, D. Estrada, and E. Pop, "Low-power switching of phase-change materials with carbon nanotube electrodes," *Science* **332**(6029), 568–570 (2011).
22. H. Zhang, L. Zhou, L. Lu, J. Xu, N. Wang, H. Hu, B. M. A. Rahman, Z. Zhou, and J. Chen, "Miniature multilevel optical memristive switch using phase change material," *ACS Photonics* **6**(9), 2205–2212 (2019).
23. H. Zhang, L. Zhou, J. Xu, N. Wang, H. Hu, L. Lu, B. M. A. Rahman, and J. Chen, "Nonvolatile waveguide transmission tuning with electrically-driven ultra-small GST phase-change material," *Sci. Bull.* **64**(11), 782–789 (2019).
24. R. L. Cotton and J. Siegel, "Stimulated crystallization of melt-quenched Ge₂Sb₂Te₅ films employing femtosecond laser double pulses," *J. Appl. Phys.* **112**(12), 123520 (2012).
25. M. Stegmaier, C. Ríos, H. Bhaskaran, C. D. Wright, and W. H. P. Pernice, "Nonvolatile all-optical 1×2 switch for chip-scale photonic networks," *Adv. Opt. Mater.* **5**(1), 1600346–7 (2017).
26. Q. Zhang, Y. Zhang, J. Li, R. Soref, T. Gu, and J. Hu, "Broadband nonvolatile photonic switching based on optical phase change materials: beyond the classical figure-of-merit," *Opt. Lett.* **43**(1), 94–97 (2018).
27. Z. Yu, J. Zheng, P. Xu, W. Zhang, and Y. Wu, "Ultracompact electro-optical modulator-based Ge₂Sb₂Te₅ on silicon," *IEEE Photonics Technol. Lett.* **30**(3), 250–253 (2018).
28. W. H. P. Pernice and H. Bhaskaran, "Photonic non-volatile memories using phase change materials," *Appl. Phys. Lett.* **101**(17), 171101 (2012).
29. C. Ríos, P. Hosseini, C. D. Wright, H. Bhaskaran, and W. H. P. Pernice, "On-chip photonic memory elements employing phase-change materials," *Adv. Mater.* **26**(9), 1372–1377 (2014).
30. C. Ríos, M. Stegmaier, P. Hosseini, D. Wang, T. Scherer, C. D. Wright, H. Bhaskaran, and W. H. P. Pernice, "Integrated all-photonic non-volatile multi-level memory," *Nat. Photonics* **9**(11), 725–732 (2015).
31. C. Ríos, N. Youngblood, Z. Cheng, M. Le Gallo, W. H. P. Pernice, C. D. Wright, A. Sebastian, and H. Bhaskaran, "In-memory computing on a photonic platform," *Sci. Adv.* **5**(2), eaa5759 (2019).
32. Z. Cheng, C. Ríos, W. H. P. Pernice, C. D. Wright, and H. Bhaskaran, "On-chip photonic synapse," *Sci. Adv.* **3**(9), e1700160 (2017).
33. J. Feldmann, M. Stegmaier, N. Gruhler, C. Ríos, H. Bhaskaran, C. D. Wright, and W. H. P. Pernice, "Calculating with light using a chip-scale all-optical abacus," *Nat. Commun.* **8**(1), 1256 (2017).

34. J. Zheng, A. Khanolkar, P. Xu, S. Colburn, S. Deshmukh, J. Myers, J. Frantz, E. Pop, J. Hendrickson, J. Doylend, N. Boechler, and A. Majumdar, "GST-on-silicon hybrid nanophotonic integrated circuits: a nonvolatile quasi-continuously reprogrammable platform," *Opt. Mater. Express* **8**(6), 1551–1561 (2018).
35. P. Xu, J. Zheng, J. K. Doylend, and A. Majumdar, "Low-loss and broadband nonvolatile phase change directional coupler switches," *ACS Photonics* **6**(2), 553–557 (2019).
36. R. Boeck, W. Shi, L. Chrostowski, and N. A. F. Jaeger, "FSR-eliminated Vernier racetrack resonators using grating-assisted couplers," *IEEE Photonics J.* **5**(5), 2202511 (2013).
37. S. M. Rytov, "Electromagnetic properties of a finely stratified medium," *Sov. Phys. JETP* **2**, 466–475 (1956).
38. P. Yeh and H. F. Taylor, "Contradirectional frequency-selective couplers for guided-wave optics," *Appl. Opt.* **19**(16), 2848–2855 (1980).
39. W. Shi, H. Yun, C. Lin, J. Flueckiger, N. A. F. Jaeger, and L. Chrostowski, "Coupler-apodized Bragg-grating add-drop filter," *Opt. Lett.* **38**(16), 3068–3070 (2013).
40. N. Yokoi, T. Fujisawa, K. Saitoh, and M. Koshiba, "Apodized photonic crystal waveguide gratings," *Opt. Express* **14**(10), 4459–4468 (2006).